Supplementary Information (SI) for RSC Advances.

Strain Effects of Catalytic Activity and Stability of PdM Nanoalloys with grain boundary

Junpeng Wang,[a, b] *Tao Jin,*[c] *Longfei Guo,*[a, b] *Zhen Li*[a, b] *Chongyang Wang,*[a, b] *Shuang Shan,*[a, b] *Quan Tang,*[a, b] *Bowei Pan,*[a, b] *and Fuyi Chen*[*, a, b]

[a] State Key Laboratory of Solidification Processing, Northwestern Polytechnical University, Xi'an 710072, China

[b] School of Materials Science and Engineering, Northwestern Polytechnical University, Xi'an, 710072, China

[c] Longmen Laboratory, Luoyang, 471000, China

[*]Corresponding author: E-mail: fuyichen@nwpu.edu.cn

Details of thermodynamic calculations

We examined the catalytic activity of PdM (M = Ir, Ag) nanoalloys for formate dehydrogenation (FDH) and formic acid oxidation (FOR) through Gibbs free energy calculations. Additionally, we utilized the Nørskov[1]

method to investigate the effects of the electric potential on the activity and mechanism of the FOR:

$$\Delta G = \Delta H - T\Delta S = \Delta E + \Delta ZPE - T\Delta S + \Delta G_U + \Delta G_{pH} + \Delta G_{field}$$

where ΔE is the DFT total energy, T is the temperature (298.15 K), ΔZPE and ΔS are the change in zero-point energy and entropy of the adsorbates, respectively. ΔG_U is the electrode potential ($\Delta G_U = eU$, where U is the electrode potential with respect to the standard hydrogen electrode and e is the transferred charge). ΔG_{pH} is the pH value of the electrolyte ($\Delta G_{pH} =- k_B T \cdot \ln 10 \times pH$, where k_B is the Boltzmann constant). We used pH = 14 for an alkaline medium because of our experimental environment for FOR. ΔG_{field} is the free energy correction caused by the electrochemical double layer and is normally ignored because of its small value similar to previous studies[2, 3]. The Gibbs free energy of liquid water is $\Delta G_{H_2O(l)} = \Delta G_{H_2O(g)} + RT\ln\left(p/p_0\right)$, where $\Delta G_{H_2O(g)}$ is calculated through DFT calculations, R is the ideal gas constant, p is the saturated vapor pressure (0.035 bar), p_0 is the standard pressure of 1 bar, and T is the temperature (298.15 K). The free energy of OH^- was calculated using the expression: $\Delta G_{OH^-} = \Delta G_{H_2O(l)} - G_{H^+}$, where, $G_{H^+} = 1/2 G_{H_2} - k_B T \ln 10 \times pH$.

The adsorption energy is defined as follows:

$$E_{ad} = E_{total} - E_{nanoalloy} - E_x$$

where E_{ad}, E_{total}, $E_{nanoalloy}$, and E_x represent the adsorption energy, the total energy of the cluster with an adsorbent, a clean cluster, and the gas-phase adsorbents, respectively. For the adsorption of formate ions, we placed a counter ion in the vacuum space to keep the system electrically neutral[4].

The adsorption free energy is defined as follows:

$$G_{ad} = G_{total} - E_{nanoalloy} - G_x$$

where G_{ad}, G_{total}, $E_{nanoalloy}$, and G_x represent the adsorption free energy, the free energy of the cluster with an adsorbent, the total energy of a clean cluster, and the free energy of gas-phase adsorbents, respectively.

The segregation energy of Ag@Pd and Ir@Pd nanoalloys was calculated as follows:

$$E_{seg} = E_{segregated\ alloy} - E_{alloy}$$

where the $E_{segregated\ alloy}$ and E_{alloy} is the total energy of segregated alloy and unsegregated alloy with or without adsorbate.

Detail calculation steps of atomic strain are as follows[5]:

1. The particle displacement vector U_i is calculated from the atomic coordinates of the particle in the initial and final configurations. The initial configuration is the input structure of MD simulations, and the terminated configuration is the structure after MD simulations.

2. The atomic deformation gradient tensor F is calculated for each particle.

$$F(X,t) = F_{jk} e_j \otimes I_k$$

where e_j and I_k are the unit vectors.

3. The atomic Green-Lagrangian strain tensor is calculated for each particle.

$$E = 1/2\left(F^T F - 1\right)$$

4. Calculation of atomic strain.

$$atomic\ strain = \left(E_{xx} + E_{yy} + E_{zz}\right)/3$$

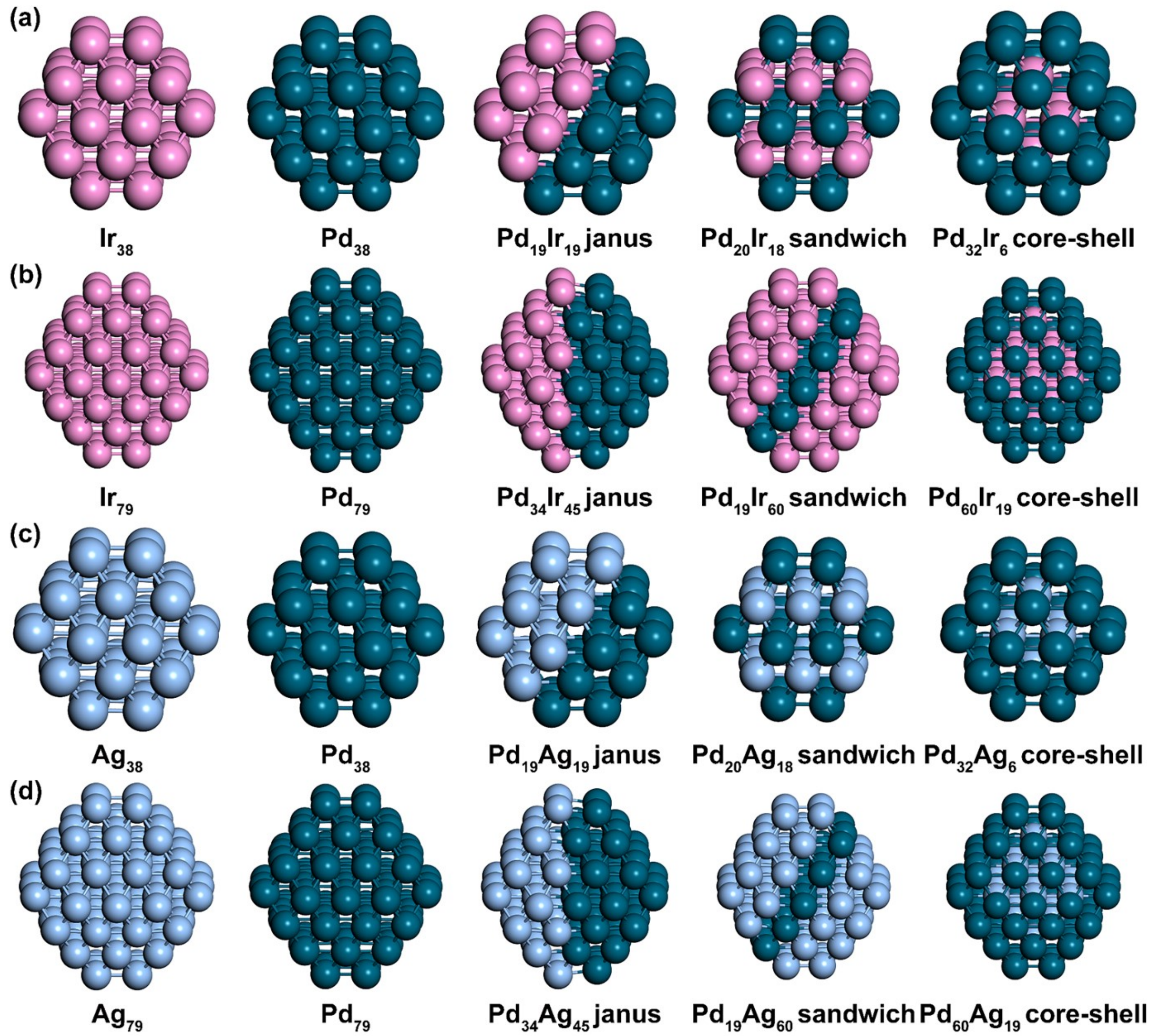

Figure S1. The atomic structure of various PdM_{38} and PdM_{79} (M = Ir, Ag) nanoalloys (a) $PdIr_{38}$, (b) $PdIr_{79}$, (c) $PdAg_{38}$ and (d) $PdAg_{79}$ nanoalloys, including Ir_{38}, Ag_{38}, Pd_{38}, Ir_{79}, Ag_{79}, Pd_{79}, $Pd_{19}M_{19}$janus, $Pd_{20}M_{18}$sandwich, $Pd_{32}M_{6}$core-shell, $Pd_{34}M_{45}$janus, $Pd_{19}M_{60}$sandwich, and $Pd_{60}M_{19}$core-shell (M = Ir, Ag) nanoalloys.

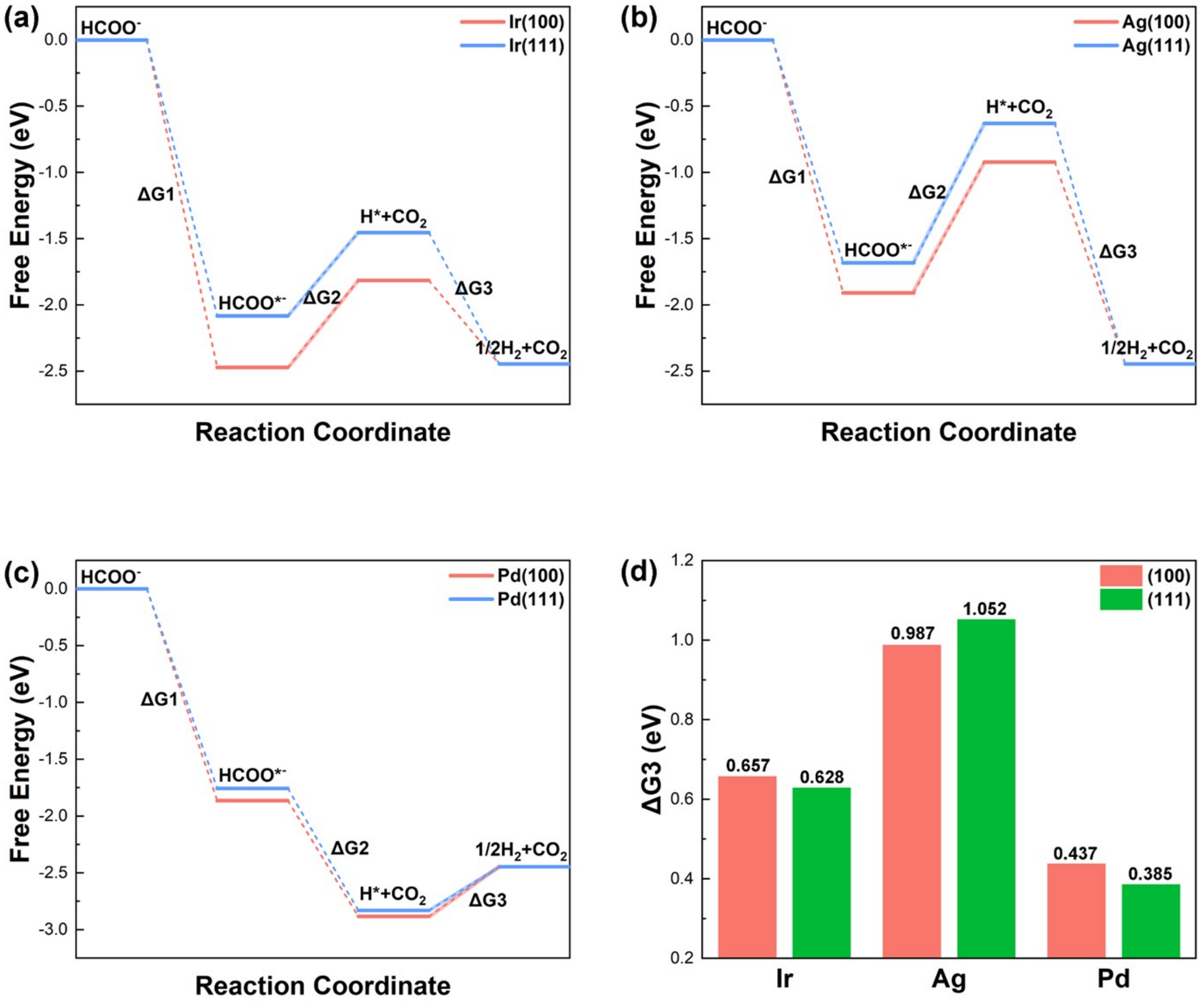

Figure S2. The free energy diagram of FDH on (a) Ir(100) and Ir(111) surfaces, (b) Ag(100) and Ag(111) surfaces, and (c) Pd(100) and Pd(111) surfaces. (d) The ΔG3 of FDH on the M(100) and M(111) surfaces (M = Ir, Ag and Pd).

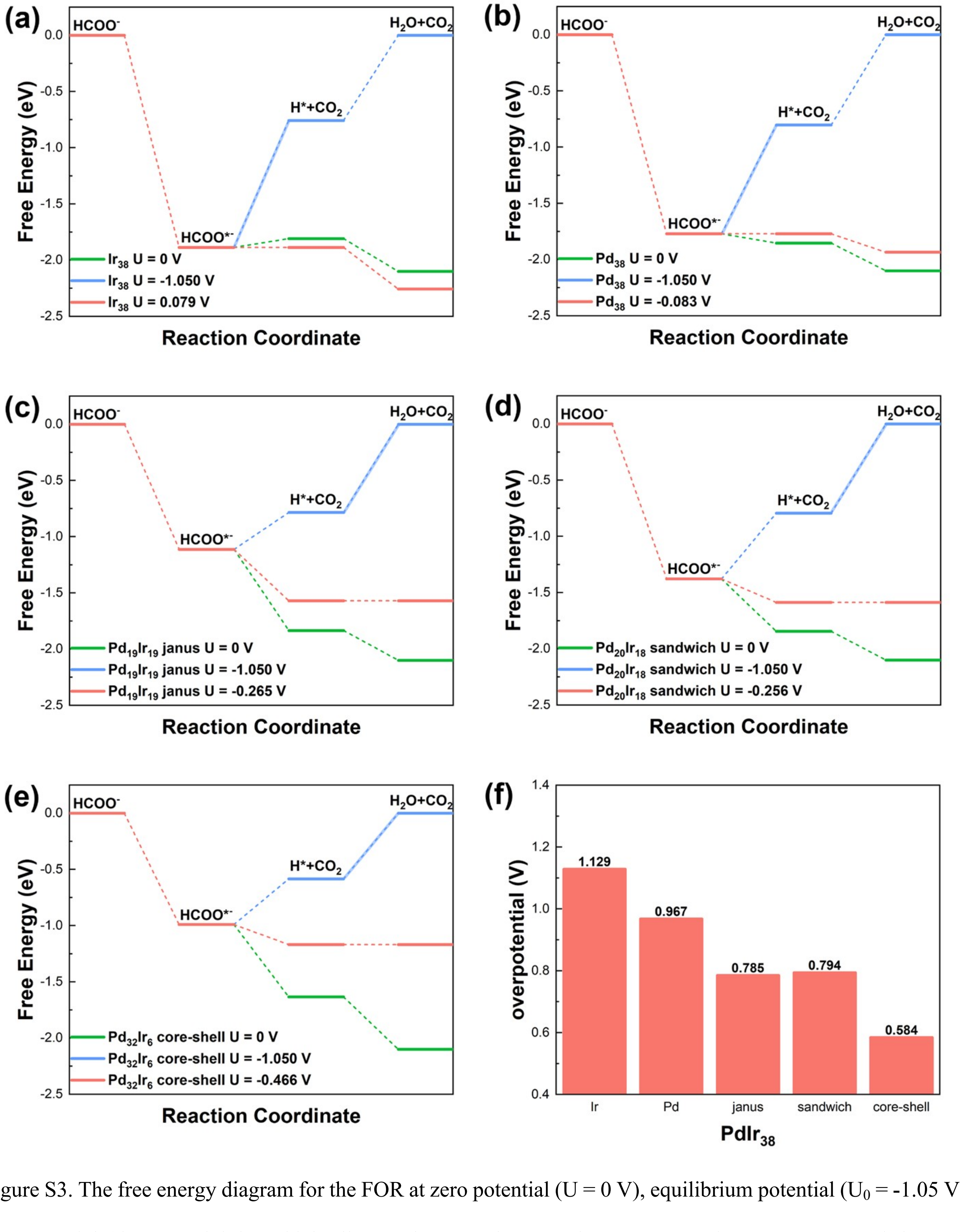

Figure S3. The free energy diagram for the FOR at zero potential (U = 0 V), equilibrium potential (U_0 = -1.05 V), overpotential (the potential for which all steps become downwards at pH 14 and T=298.15 K) and the FOR overpotential on $PdIr_{38}$ nanoalloy.

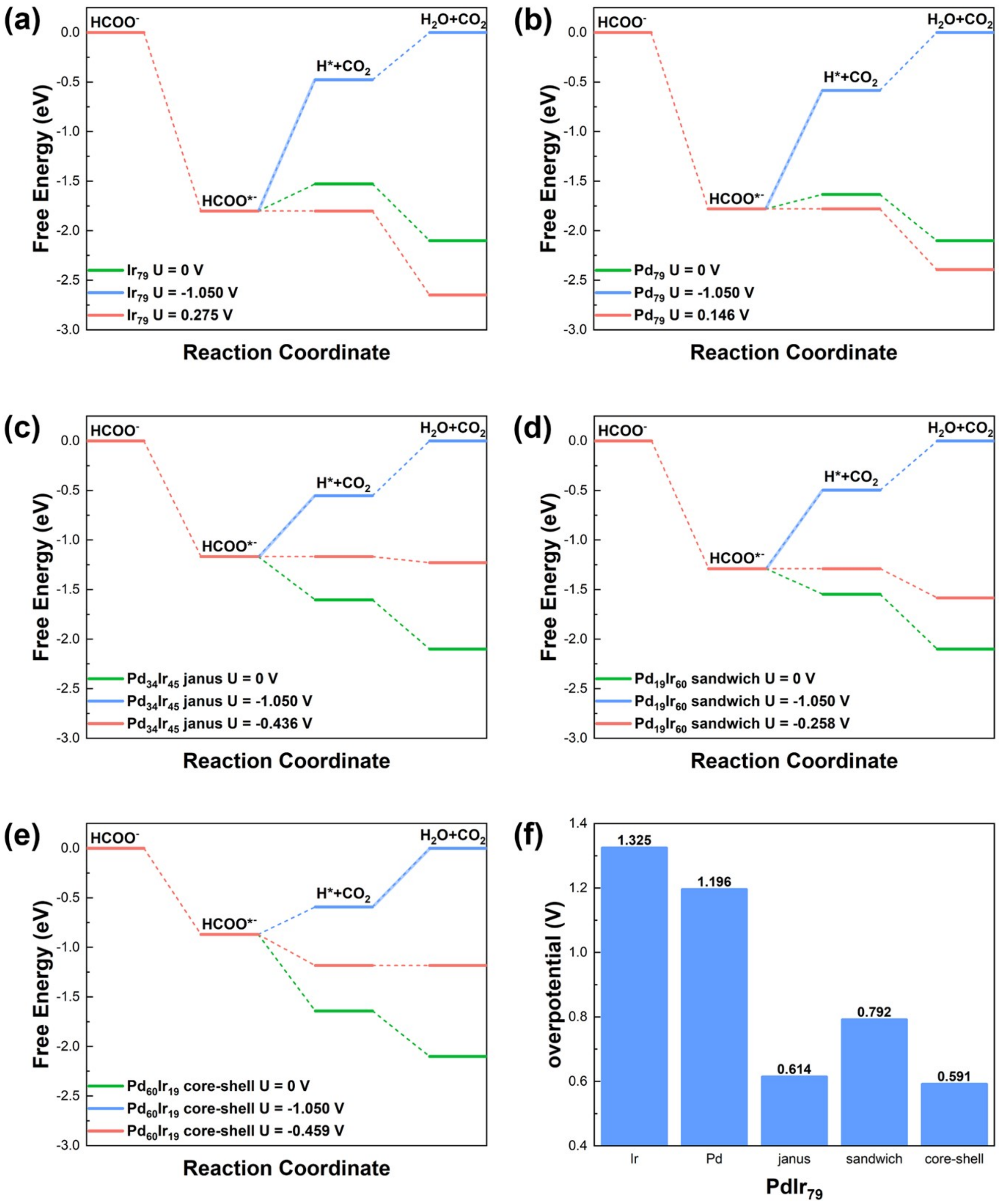

Figure S4. The free energy diagram for the FOR at zero potential (U = 0 V), equilibrium potential (U_0 = -1.05 V), overpotential (the potential for which all steps become downwards at pH 14 and T=298.15 K) and the FOR overpotential on $PdIr_{79}$ nanoalloy.

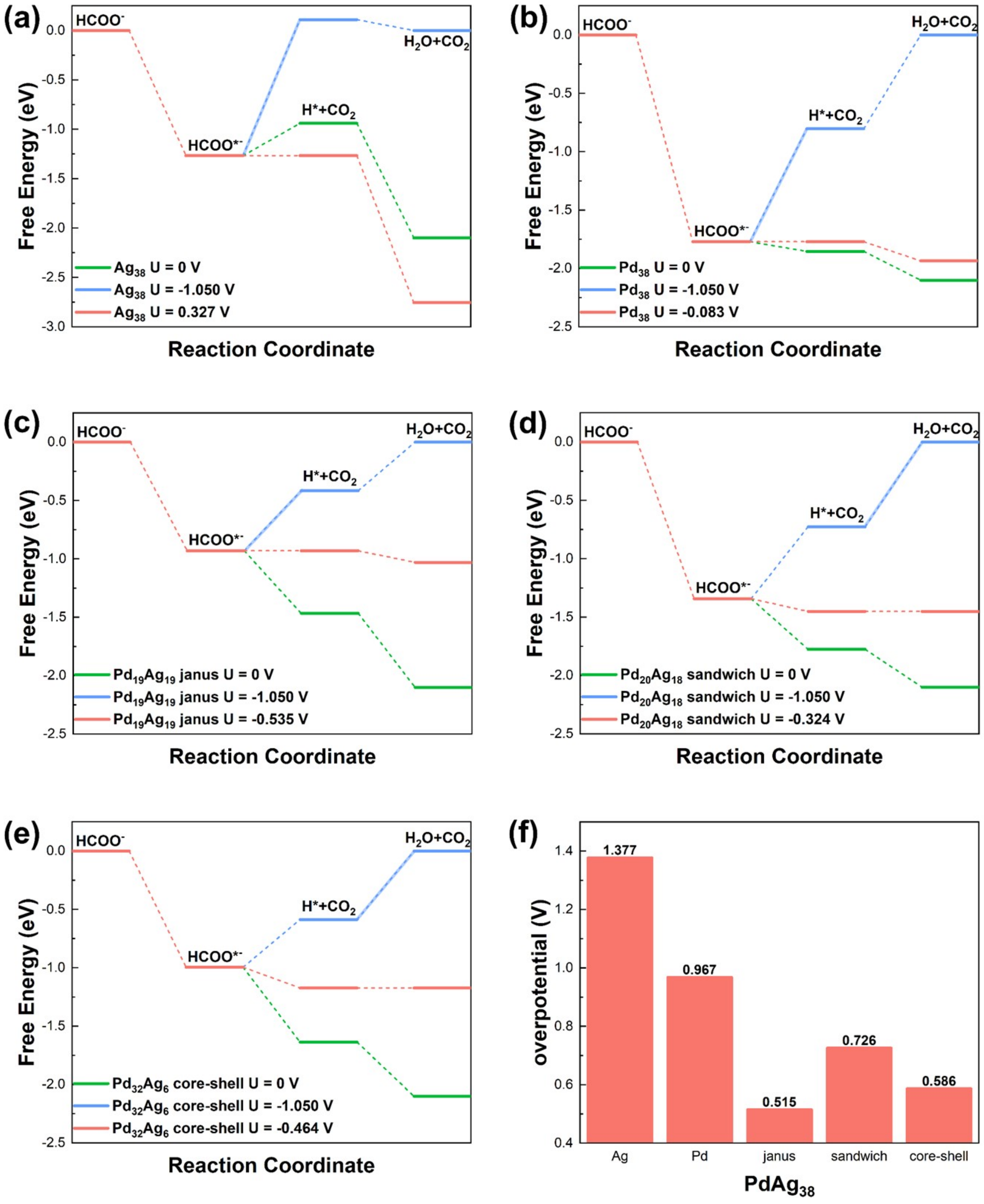

Figure S5. The free energy diagram for the FOR at zero potential (U = 0 V), equilibrium potential (U_0 = -1.05 V), overpotential (the potential for which all steps become downwards at pH 14 and T=298.15 K) and the FOR overpotential on $PdAg_{38}$ nanoalloy.

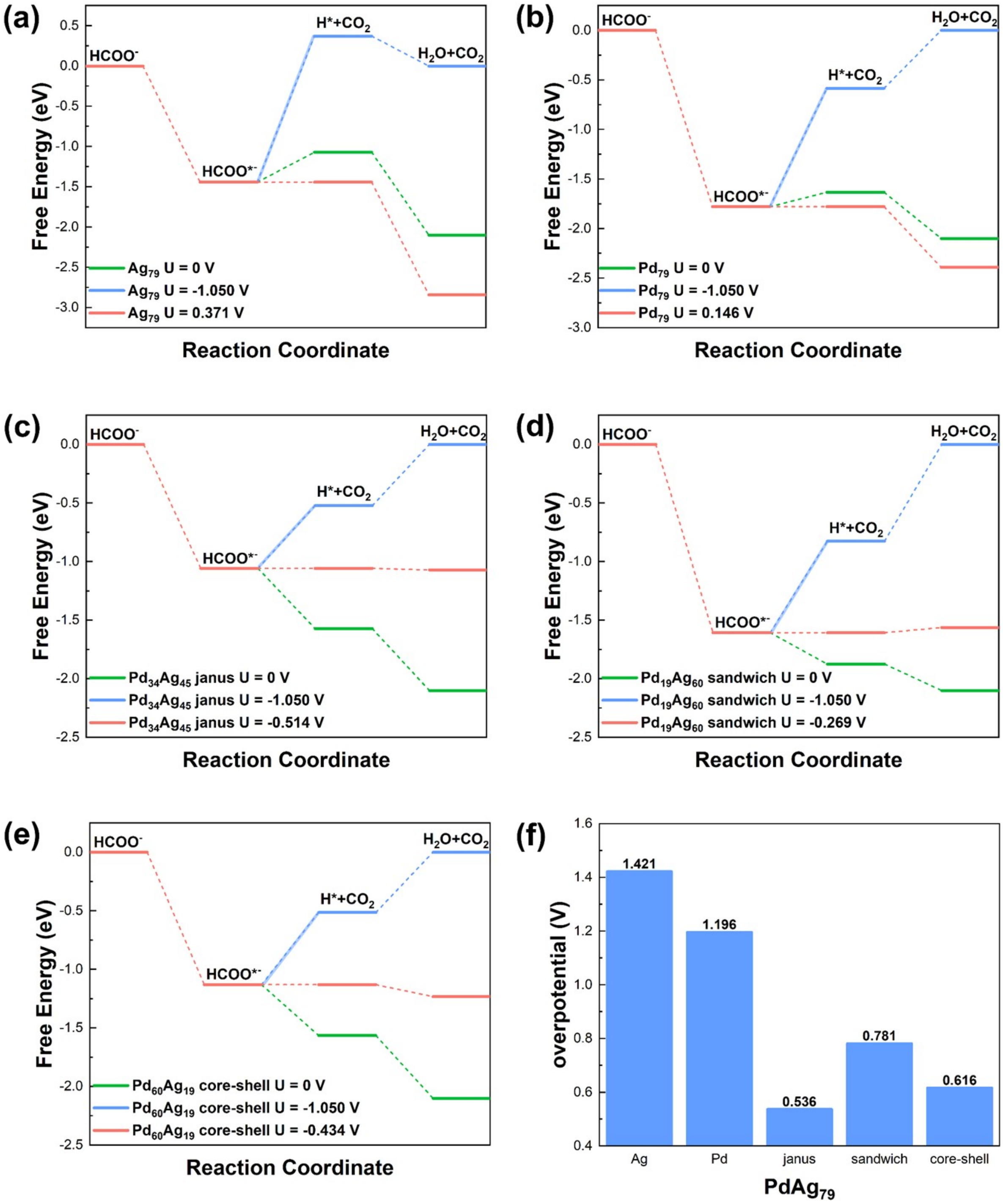

Figure S6. The free energy diagram for the FOR at zero potential (U = 0 V), equilibrium potential (U_0 = -1.05 V), overpotential (the potential for which all steps become downwards at pH 14 and T=298.15 K) and the FOR overpotential on $PdAg_{79}$ nanoalloy.

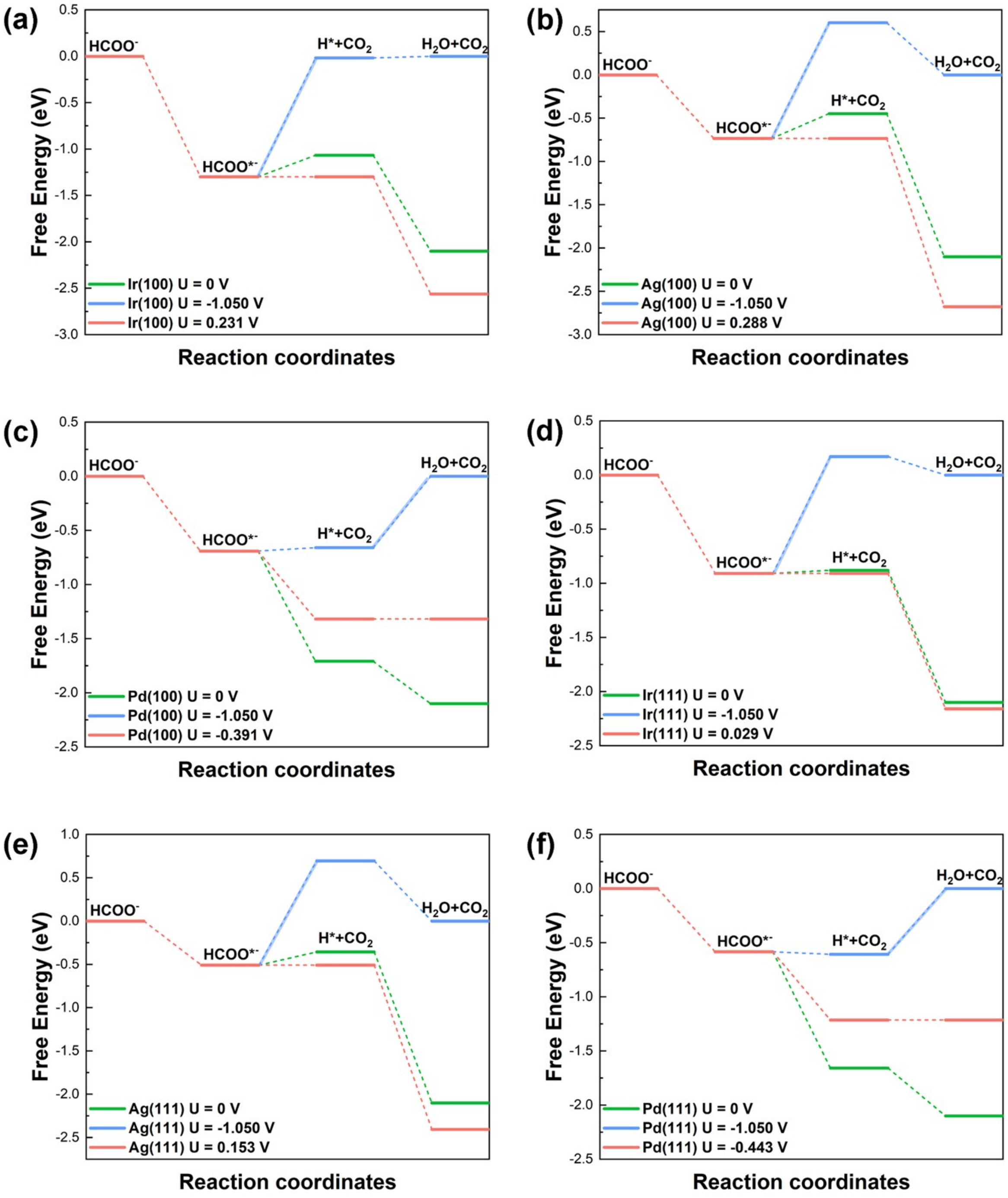

Figure S7. The free energy diagram for the FOR at zero potential (U = 0 V), equilibrium potential (U_0 = -1.05 V), overpotential (the potential for which all steps become downwards at pH 14 and T=298.15 K) and the FOR overpotential on M(100) and M(111) surfaces (M = Ir, Ag and Pd).

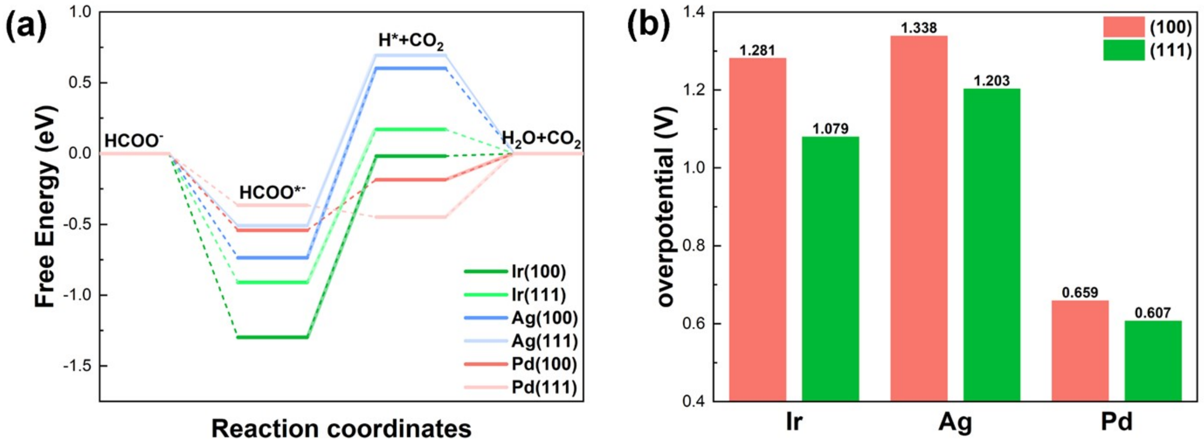

Figure S8. (a) The free energy diagram of FOR on M(100) and M(111) surfaces (M = Ir, Ag and Pd) at equilibrium potential (U_0 = -1.05 V). (b) The overpotential for formate oxidation reactions of M(100) and M(111) surfaces (M = Ir, Ag and Pd).

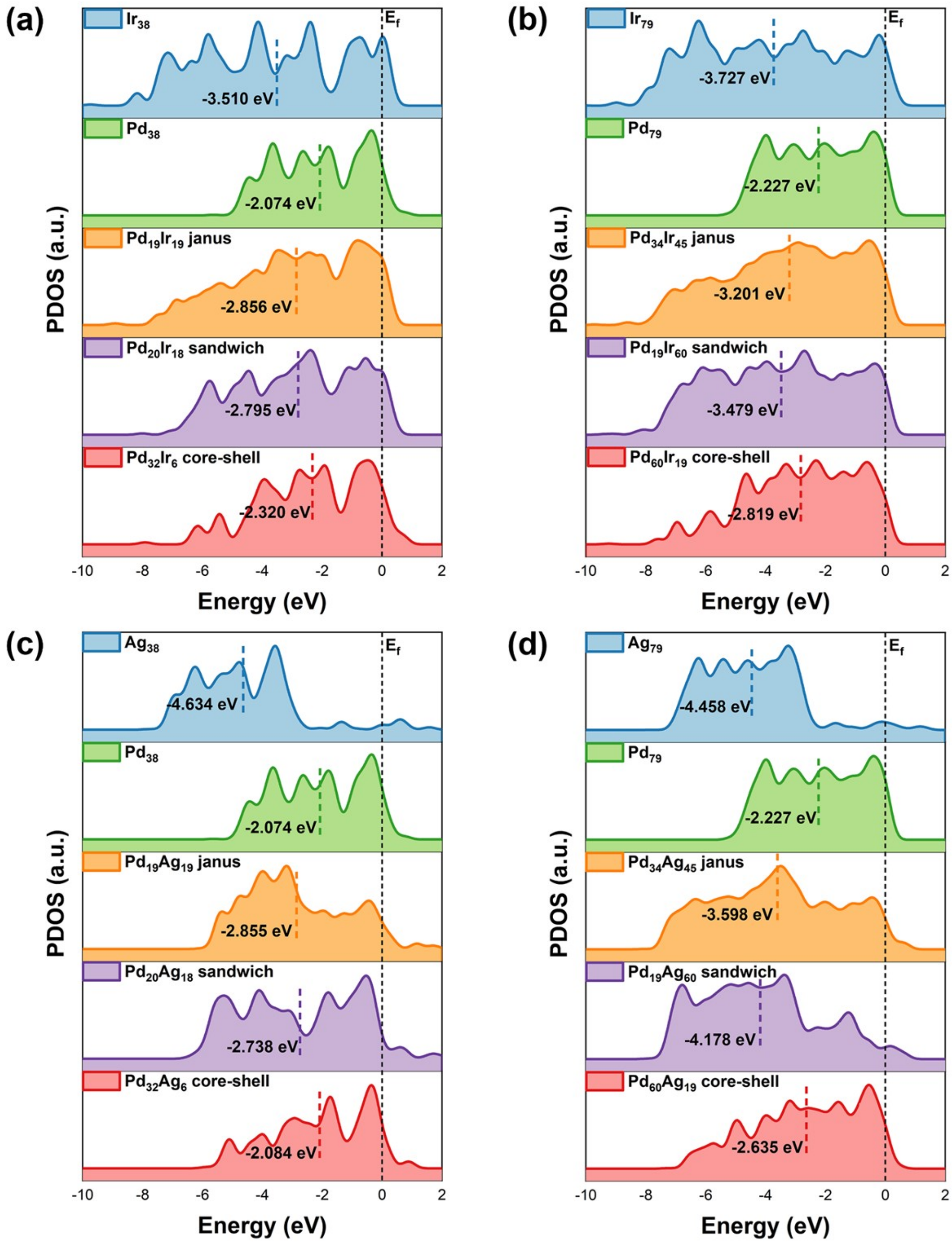

Figure S9. The projected density of states (PDOS) and d-band centers of PdM_{38} and PdM_{79} (M = Ir, Ag) nanoalloys, containing Ir_{38}, Ag_{38}, Pd_{38}, Ir_{79}, Pd_{79}, $Pd_{19}M_{19}$janus, $Pd_{20}M_{18}$sandwich, $Pd_{32}M_{6}$core-shell, $Pd_{34}M_{45}$janus, $Pd_{19}M_{60}$sandwich and $Pd_{60}M_{19}$core-shell (M = Ir, Ag) nanoalloys. The Fermi energy level is denoted as E_f.

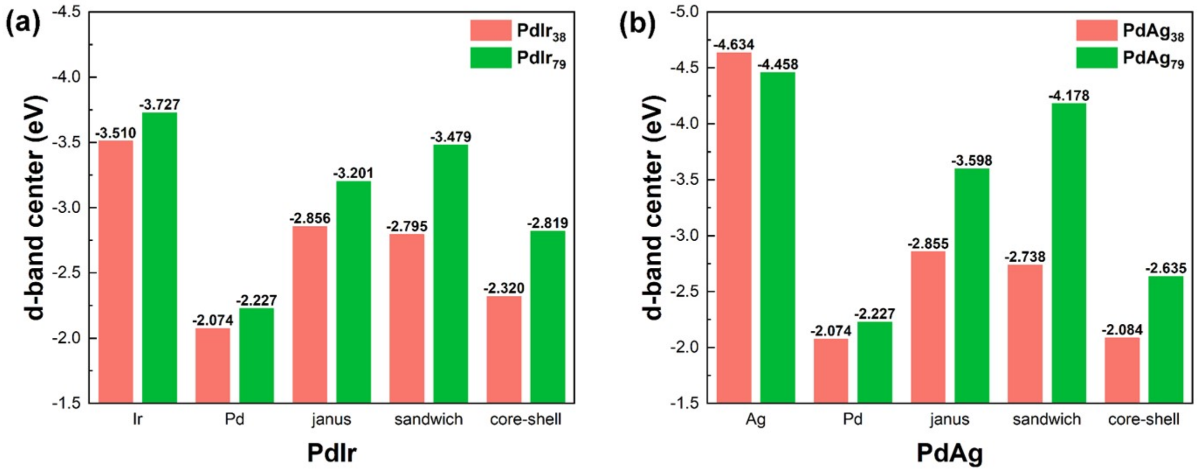

Figure S10. The d-band center of (a) $PdIr_{38}$ and $PdIr_{79}$, (b) $PdAg_{38}$ and $PdAg_{79}$ nanoalloys.

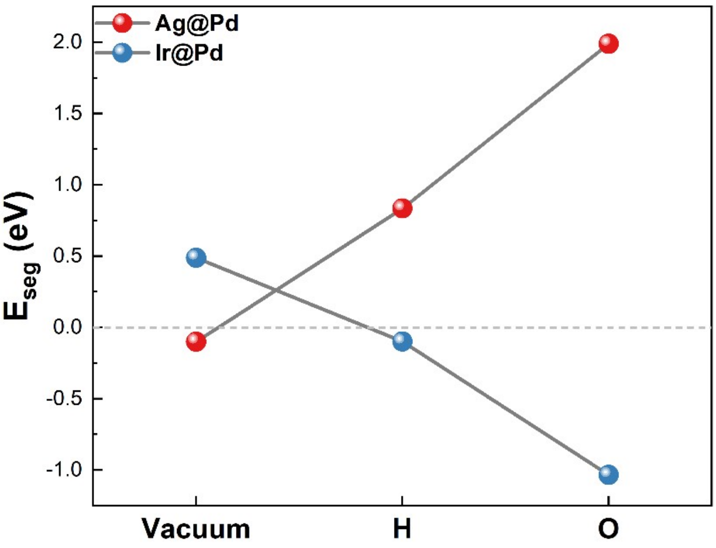

Figure S11. The segregation energy of Ag@Pd and Ir@Pd nanoalloys under vacuum, and under the adsorption of H, and O. Ag@Pd core-shell alloys exhibit a preference for Ag surface segregation in vacuum conditions, however, it is important to note that the thermodynamic feasibility of Ag surface segregation diminishes once H intermediates are formed during formate dehydrogenation and oxidation reactions. Ir@Pd core-shell alloys exhibit without Ir surface segregation in vacuum conditions, however, it is important to note that the thermodynamic feasibility of Ir surface segregation diminishes once H intermediates are formed during formate dehydrogenation and oxidation reactions.

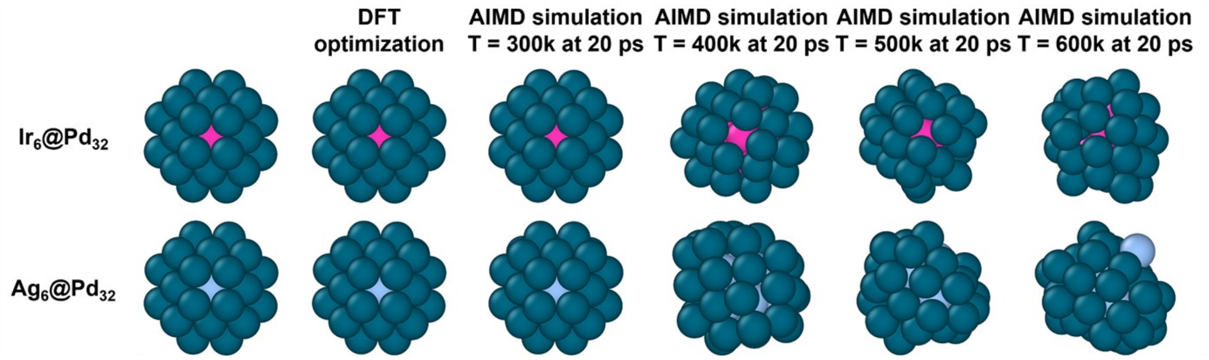

Figure S12. Atomic structure evolution of PdM core-shell (M = Ir, Ag) nanoalloys with varying temperature.

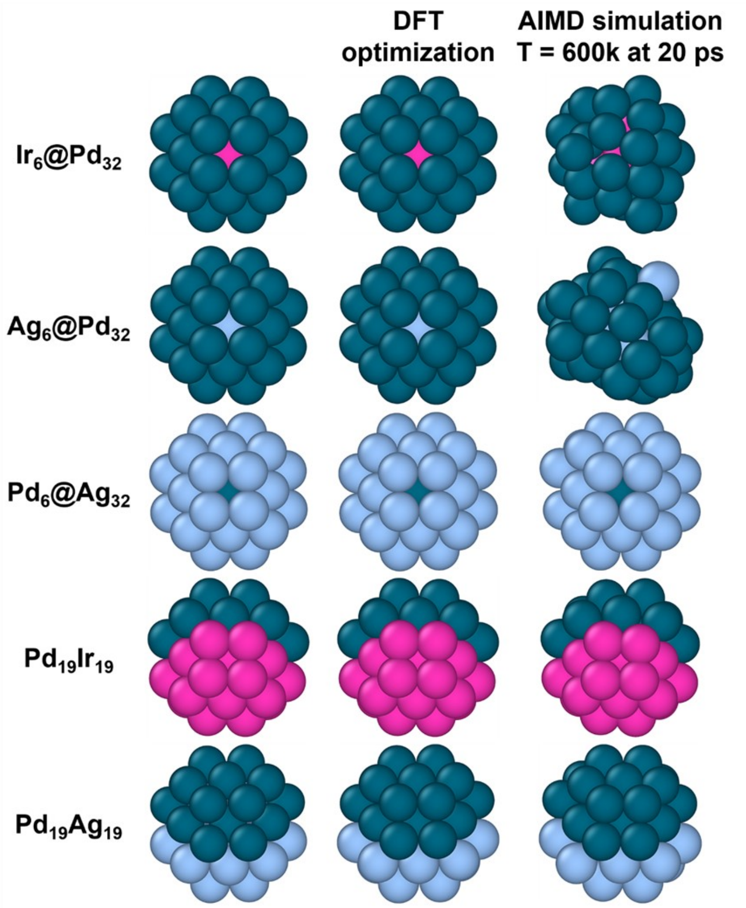

Figure S13. Atomic structure of PdM core-shell and PdM janus (M = Ir, Ag) nanoalloys after DFT optimization and AIMD simulation at 600 K.

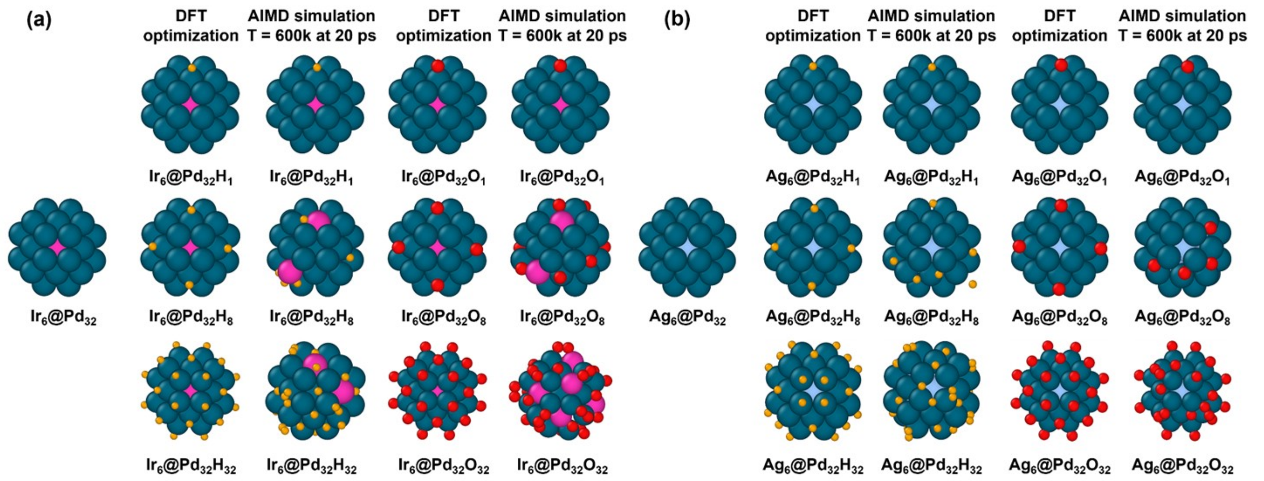

Figure S14. Atomic structure evolution of PdM core-shell (M = Ir, Ag) nanoalloys after adsorption of hydrogen and oxygen atoms with varying coverage, investigated using DFT optimization and AIMD simulations at 600 K. Ir atoms are segregated from core to shell after AIMD simulation when H and O atom coverage is high. The locations marked by white circles are Ir atoms which segregate to the shell.

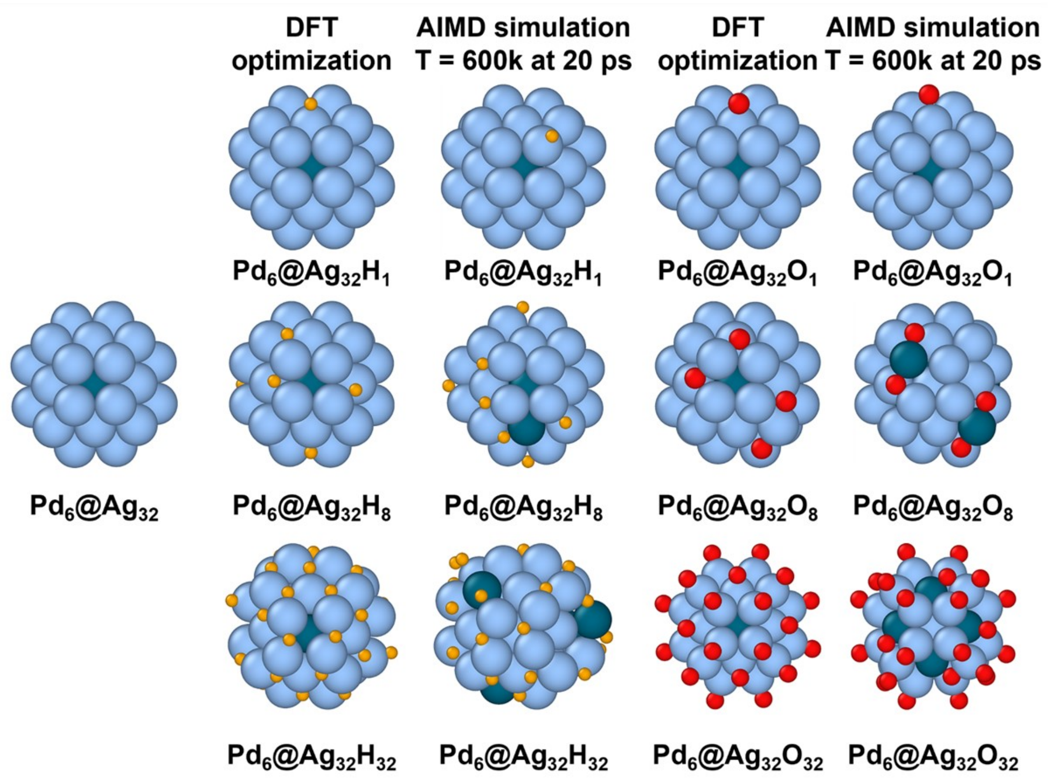

Figure S15. Atomic structure evolution of PdAg core-shell nanoalloy after adsorption of hydrogen and oxygen atoms with varying coverage, investigated using DFT optimization and AIMD simulations at 600 K. Pd atoms are segregated from core to shell after AIMD simulation when H and O atom coverage is high.

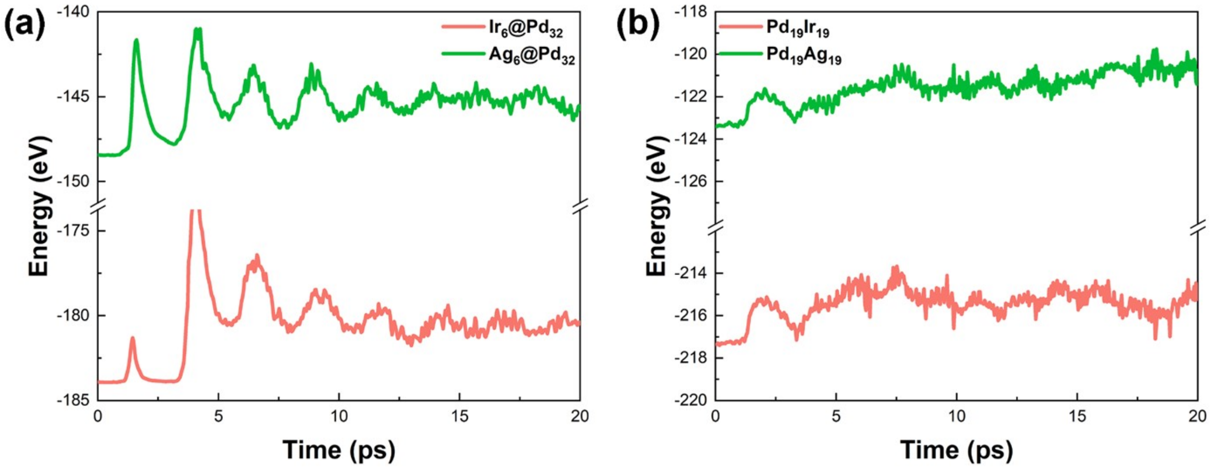

Figure S16. The total energy versus the time for AIMD simulations of the (a) Ir_6@Pd_{32} and Ag_6@Pd_{32} nanoalloy, and (b) $Pd_{19}Ir_{19}$ and $Pd_{19}Ag_{19}$janus nanoalloy under vacuum.

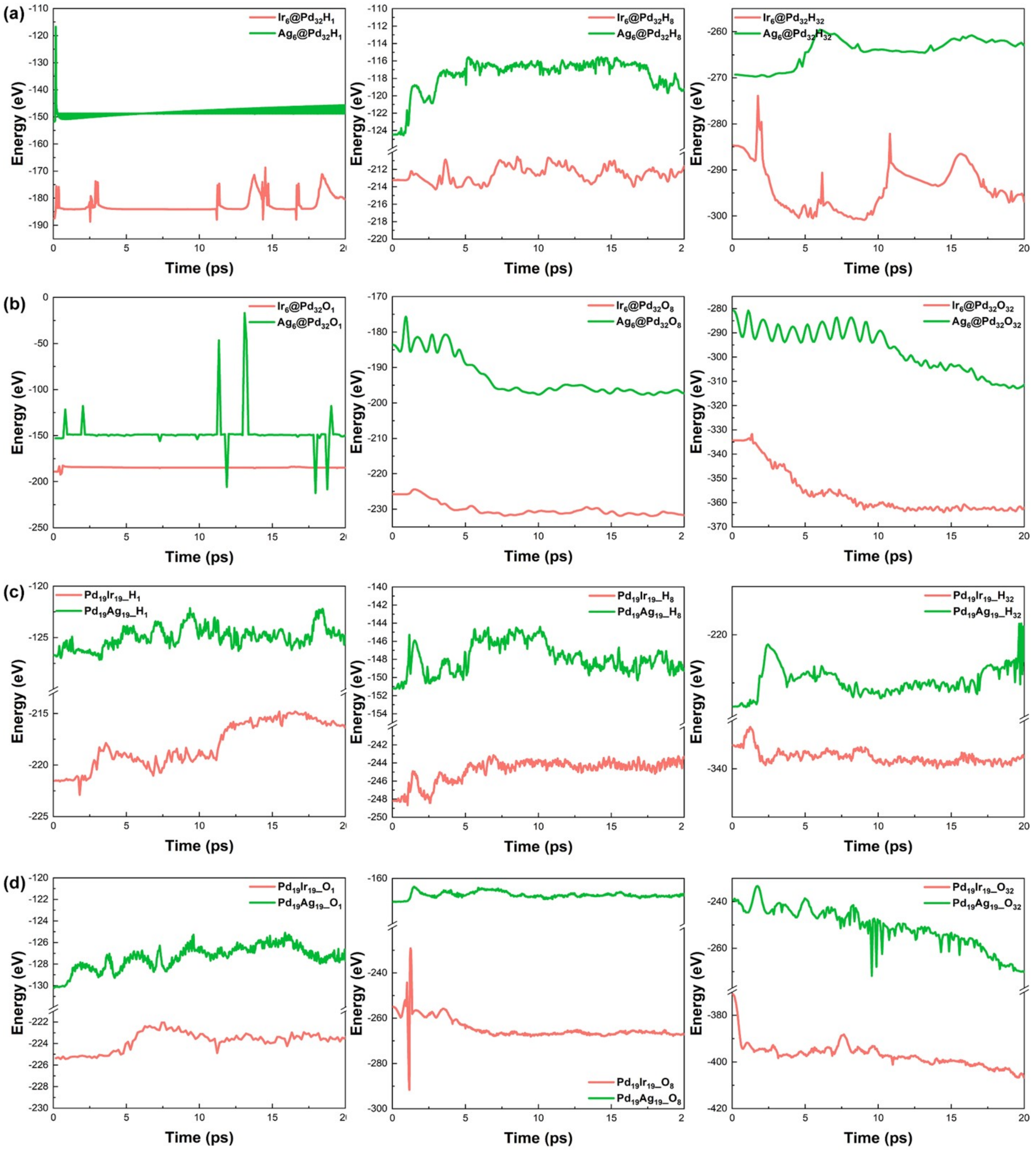

Figure S17. The total energy versus the time for AIMD simulations of the (a) $Ir_6@Pd_{32}$ and $Ag_6@Pd_{32}$ nanoalloy under H atom environment, (b) $Ir_6@Pd_{32}$ and $Ag_6@Pd_{32}$ nanoalloy under O atom environment, (c) $Pd_{19}Ir_{19}$ and $Pd_{19}Ag_{19}$janus nanoalloy under H atom environment, and (d) $Pd_{19}Ir_{19}$ and $Pd_{19}Ag_{19}$janus nanoalloy under O atom environment.

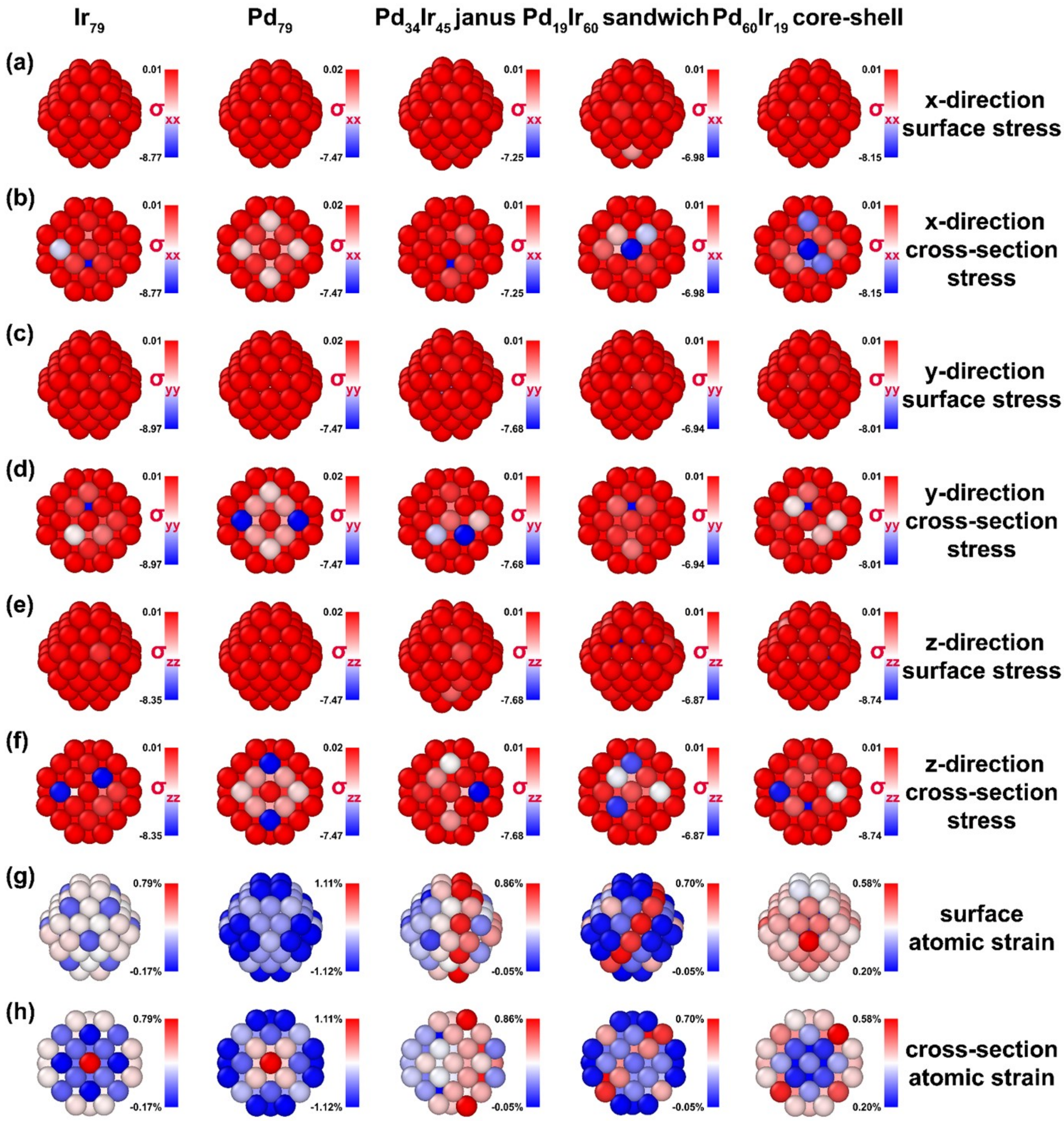

Figure S18. The stress distribution and atomic strain field maps of Ir_{79}, Pd_{79}, $Pd_{34}Ir_{45}$janus, $Pd_{19}Ir_{60}$sandwich, and $Pd_{60}Ir_{19}$core-shell nanoalloys. (a, b) The x-direction, (c, d) y-direction, and (e, f) z-direction for surface and cross-sectional stress. (g, h) The atomic strain at the surface and in the cross-section. In $Pd_{34}Ir_{45}$ Janus and $Pd_{19}Ir_{60}$ sandwich nanoalloys, Ir atoms undergo tensile strain and Pd atoms compressive strain. Stress is measured in bar. Color - maps show stress/strain: blue for compressive, red for tensile, white for zero.

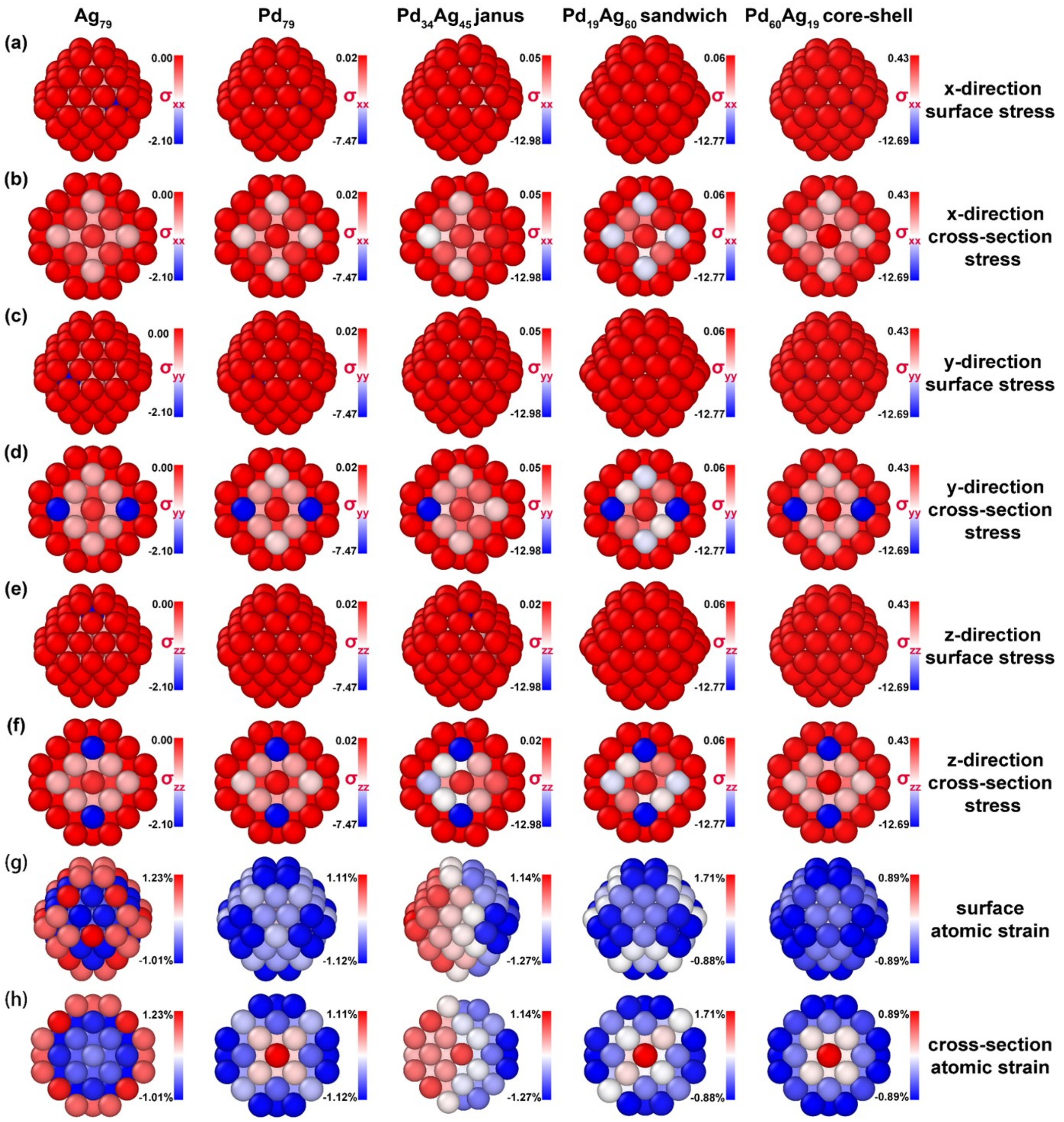

Figure S19. The stress distribution and atomic strain field maps of Ag_{79}, Pd_{79}, $Pd_{34}Ag_{45}$janus, $Pd_{19}Ag_{60}$sandwich, and $Pd_{60}Ag_{19}$core-shell nanoalloys. (a, b) The x-direction, (c, d) y-direction, and (e, f) z-direction for surface and cross-sectional stress. (g, h) The atomic strain at the surface and in the cross-section. In $Pd_{34}Ag_{45}$ Janus nanoalloys, Ag atoms undergo tensile strain and Pd atoms compressive strain. $PdAg_{79}$ has higher compressive strain than $PdAg_{38}$. Stress is measured in bar. Color-maps show stress/strain: blue for compressive, red for tensile, white for zero.

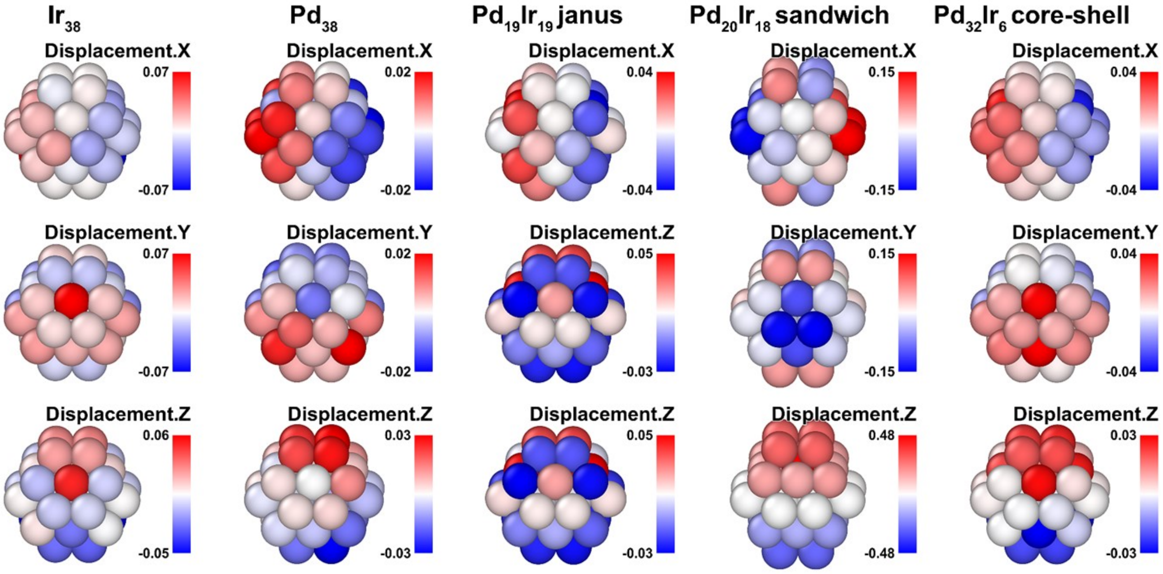

Figure S20. The displacements of PdIr$_{38}$ nanoalloys along the x, y, and z direction after MD simulations from the initial bulk and final nanoalloy configurations.

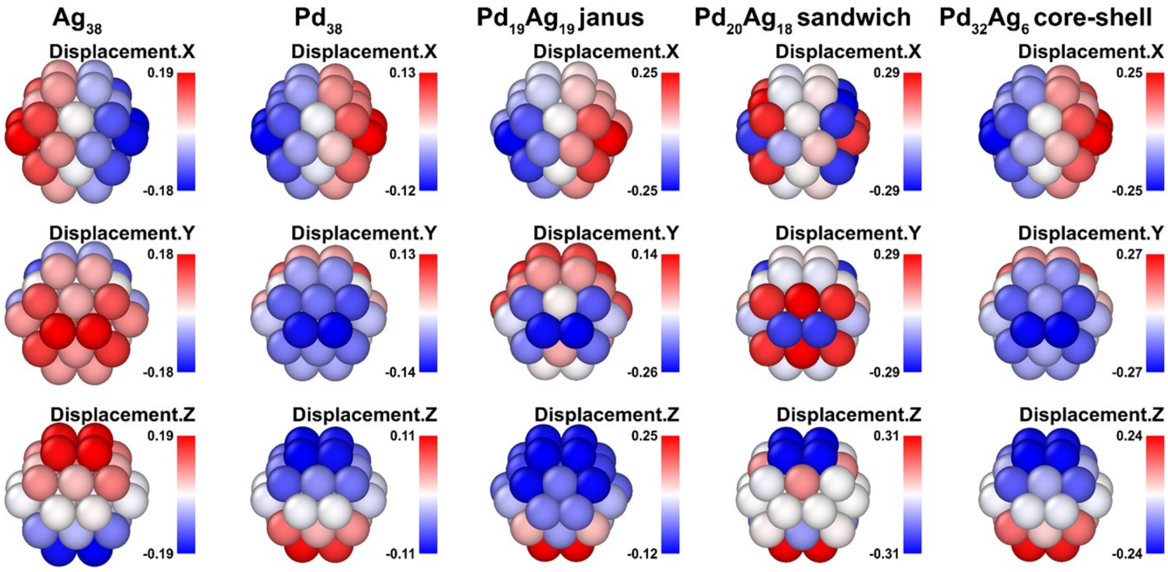

Figure S21. The displacements of PdAg$_{38}$ nanoalloys along the x, y, and z direction after MD simulations from the initial bulk and final nanoalloy configurations.

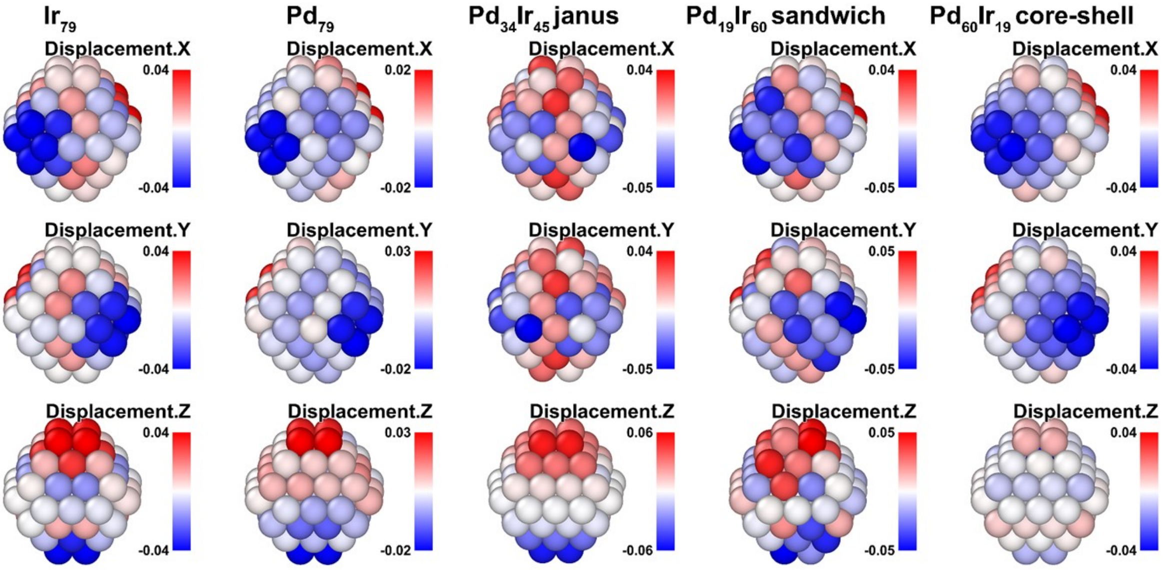

Figure S22. The displacements of $PdIr_{79}$ nanoalloys along the x, y, and z direction after MD simulations from the initial bulk and final nanoalloy configurations.

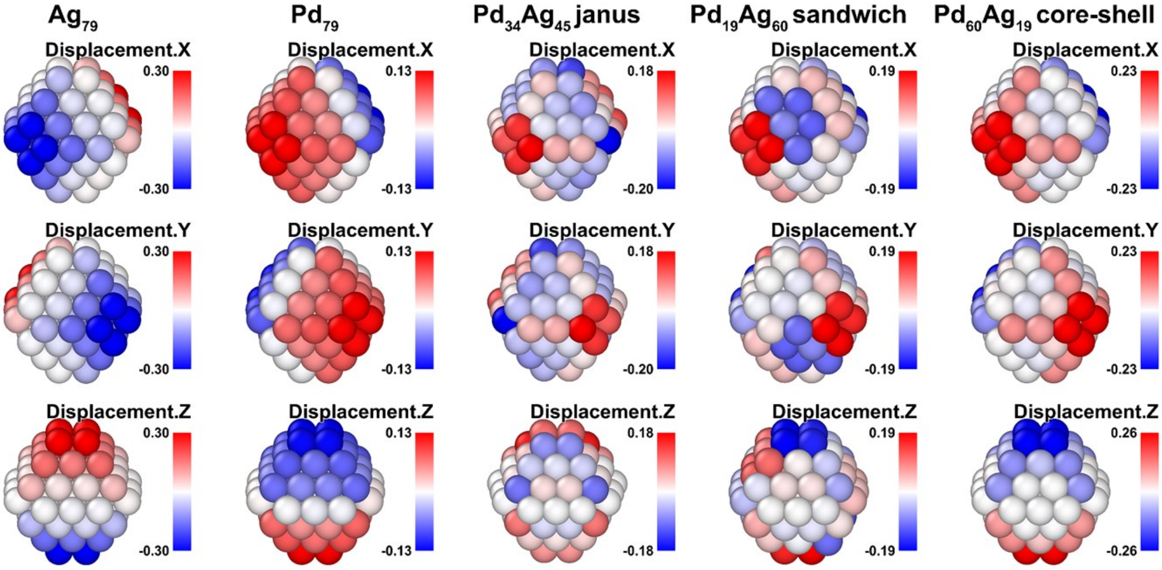

Figure S23. The displacements of $PdIr_{79}$ nanoalloys along the x, y, and z direction after MD simulations from the initial bulk and final nanoalloy configurations.

Reference

1. J. K. Nørskov, J. Rossmeisl, A. Logadottir, L. Lindqvist, J. R. Kitchin, T. Bligaard and H. Jónsson, *J. Phys. Chem. B*, 2004, **108**, 17886-17892.

2. N. Zhang, F. Chen, X. Wu, Q. Wang, A. Qaseem and Z. Xia, *J. Mater. Chem. A*, 2017, **5**, 7043-7054.

3. I. C. Man, H.-Y. Su, F. Calle-Vallejo, H. A. Hansen, J. I. Martínez, N. G. Inoglu, J. Kitchin, T. F. Jaramillo, J. K. Nørskov and J. Rossmeisl, *ChemCatChem*, 2011, **3**, 1159-1165.

4. B. R. Karimadom, D. Meyerstein and H. Kornweitz, *Phys. Chem. Chem. Phys.*, 2021, **23**, 25667-25678.

5. A. Stukowski, *Model. Simul. Mater. Sci. Eng.*, 2010, **18**, 015012.